

SOFIA/upGREAT far-infrared spectroscopy of bright rimmed pillars in IC 1848

Dariusz C. Lis¹, Rolf Güsten², Paul F. Goldsmith¹, Yoko Okada³, Youngmin Seo¹, Helmut Wiesemeyer², and Marc Mertens^{2,3}

¹ Jet Propulsion Laboratory, California Institute of Technology, 4800 Oak Drove Drive, Pasadena, CA 91109, USA

² Max-Planck-Institut für Radioastronomie, Auf dem Hügel 69, D-53121 Bonn, Germany

³ I. Physikalisches Institut, Universität zu Köln, Zùlpicher Straße 77, 50937 Köln, Germany

Received 1 August 2024 / Accepted 25 September 2024 / ©2024 All rights reserved.

ABSTRACT

Using the upGREAT instrument on SOFIA, we have imaged the [C II] 158 μm fine structure line emission in bright-rimmed pillars located at the southern edge of the IC1848 H II region, and carried out pointed observations of the [O I] 63 and 145 μm fine structure lines toward selected positions. The observations are used to characterize the morphology, velocity field, and the physical conditions in the G1–G3 filaments. The velocity-resolved [C II] spectra show evidence of a velocity shift at the head of the brightest G1 filament, possibly caused by radiation pressure from the impinging UV photons or the rocket effect of the evaporating gas. Archival *Herschel* PACS and SPIRE data imply H₂ column densities in the range $10^{21} - 10^{22} \text{ cm}^{-2}$, corresponding to maximum visual extinction $A_V \approx 10$ mag, and average H₂ volume density of $\approx 4500 \text{ cm}^{-3}$ in the filaments. The [C II] emission traces $\sim 17\%$ of the total H₂ column density, as derived from dust SED fits. PDR models are unable to explain the observed line intensities of the two [O I] fine structure lines in IC1848, with the observed [O I] 145 μm line being too strong compared to the model predictions. The [O I] lines in IC1848 are overall weak and the signal-to-noise ratio is limited. However, our observations suggest that the [O I] 63/145 μm intensity ratio is a sensitive probe of the physical conditions in photon dominated regions such as IC1848. These lines are thus excellent targets for future high-altitude balloon instruments, less affected by telluric absorption.

Key words. stars: formation – ISM: photon-dominated region (PDR) — ISM: atoms – ISM: clouds – ISM: kinematics and dynamics – ISM: individual (IC 1848)

1. Introduction

The interaction of high-mass stars with their environment determines the rate of star formation and star formation efficiency of molecular clouds, and regulates the evolution of galaxies. Mechanical and radiative energy input from high-mass stars can stir up, ionize, and heat the gas, leading to the disruption of the natal molecular cloud within a few free-fall times (see Schneider et al. 2020, and references therein.) However, high-mass stars can also provide positive feedback, by compressing the gas and allowing gravity to overcome the turbulent and magnetic support that had prevented collapse and star formation.

The aim of the SOFIA FEEDBACK legacy program (Schneider et al., 2020; Tiwari et al., 2022; Schneider et al., 2023) was to quantify the effects of stellar feedback in a range of environments ranging from single OB stars, to small groups, to rich young clusters, and to mini-starburst complexes, by determining the physical conditions using observations of the far-infrared [C II] and [O I] fine structure lines, combined with H₂ line observations from *Spitzer*, and ground-based millimeter wave observations.

Photon-Dominated Regions (PDRs), the surface layers of molecular clouds exposed to strong fluxes of UV photons, dominate the IR spectra of star-forming clouds and galaxies, and provide a unique tool to study in detail the physical and chemical processes in diverse environments ranging from diffuse clouds, molecular cloud surfaces, globules, protoplanetary disks, planetary nebulae, and starburst galaxies. The JWST Early Release

Science program PDRs4All (Berné et al., 2022; Peeters et al., 2024; Berné et al., 2024) provides template datasets designed to identify key PDR characteristics in JWST spectra of star-forming regions in our Galaxy and beyond. As discussed in Berné et al. (2022), PDRs are strong emitters in the near and mid-IR, where their key diagnostic signatures include (a) the Aromatic Infrared Bands (AIBs) attributed to PAHs, (b) continuum emission from very small carbonaceous grains (VSGs), (c) ro-vibrational and pure rotational lines of H₂, and (d) emission from atomic ions (e.g., S⁺, Si⁺, Fe⁺).

Hydrodynamical numerical simulations (Mackey et al., 2010) show that shadowing of ionizing radiation by an inhomogeneous density field can form so-called elephant trunks (ETs), or pillars of dense gas without the assistance of self-gravity or of ionization front and cooling instabilities. In some cases, the head of the ET is shown to recede from the radiation source more rapidly than the shadowed trunk which has not been exposed to radiation. For dynamically forming ETs, gas streams into the shadowed trunk past the head and is thus moving faster than, or at a comparable speed to, the pillar's head. This could result in gas compression, triggering collapse and formation of next generation of stars. A combined Chandra/optical study aimed at quantifying triggered star formation in IC 1396A (Getman et al., 2012) also argues for a radiation-driven implosion process persisting over several million years. These authors argue that the contribution of the triggered star formation for the entire HII region exceeds 14 – 25% today and may have been higher over the lifetime of the HII region. Such triggering on the periphery of

HII regions may thus be a significant mode of star formation in the Galaxy.

Magnetic fields have been suggested to have a significant influence on the development of pillars around H II regions (Williams, 2007; Mackey et al., 2011). In the case of M16, submillimeter dust polarization observations have shown that the magnetic field lines are aligned with the pillars, and perpendicular to and decoupled from the field of the surrounding photo-ionized cloud (Pattle et al., 2018).

The best-known example of such a region, M16, has recently been imaged using NIRSPEC and MIRI, revealing an incredible level of detail in these ‘‘Pillars of Creation’’ (Hester et al., 1996). Karim et al. (2023) presented SOFIA and ground-based spectroscopic observations of this region. They infer that the ionized, atomic, and molecular phases are in pressure equilibrium if the atomic gas is magnetically supported. The dense clumps at the tops of the pillars are currently supported by the magnetic field, but are likely to collapse within the photoveaporation time scales. The present study focuses on IC 1848, a similar region with a lower-UV-illumination, for which an extensive set of supporting FIR continuum and line observations from *Spitzer*, SOFIA, and *Herschel* already exists.

IC 1848 is a large HII region in Cassiopea, forming part of the W5 HII region-molecular cloud complex in the Perseus Arm, at a distance 1.9 kpc (Ishida et al., 1970), consistent within uncertainties with the recent distance estimate of 2075+44–42 pc to the Cas OB 6 association, formed by W3/W4/W5, derived from the *Gaia* EDR3 release (Maíz Apellániz et al., 2022). Past observations have revealed three bright rimmed clouds on the southern edge of the HII region (Thompson et al., 2004) at a projected distance of 13 pc from HD17505, the primary O6V ionizing star. These filaments, referred to as G1 – G3 (Figure 1), are associated with recent or ongoing star formation, as evidenced by the presence of submillimeter cores and multiple YSO’s identified in 2MASS images. This strongly suggests that UV illumination may have induced the collapse of the dense molecular cores at the head of the three clouds and Thompson et al. (2004) argue that the overall morphology of the IC 1848 clouds is reasonably consistent with radiative-driven implosion models of cometary globules.

A recent study of IC 1848 (Chauhan et al., 2011) suggests that the filaments may have been caused by hydrodynamical instability of the ionization/shock front of the expanding H II region, as similar structures often show up in recent numerical simulations of the evolution of H II regions. These authors further hypothesize that this hydrodynamic instability mechanism makes a third mode of triggered star formation associated with H II regions, in addition to the two previously recognized mechanisms, collect-and-collapse of the shell accumulated around an expanding H II region and radiation-driven implosion of bright rimmed clouds that were pre-existing cloud clumps. Accurate characterization of the physical conditions in the gas, through observations combined with state-of-the-art Meudon PDR and Cloudy modeling, would provide good quantitative constraints for such models.

To characterize the physical conditions and the velocity field in the IC 1848 filaments, observations of [C II] 158 μm and [O I] 63 and 145 μm fine structure lines were carried out using the up-GREAT instrument on SOFIA. Full velocity-resolved [C II] maps of the three filaments were obtained, along with [O I] observations at selected positions.

2. Observations

During six flights between December 2019 and April 2022, all departing from Palmdale, CA, the three trunks G1 to G3 (Figure 1) were observed with the array spectrometer upGREAT¹ (Risacher et al., 2018) aboard SOFIA (Young et al., 2012). All observations were carried out on the GREAT Consortium time (total flight time 7.5 hours, including all overheads). First, the filaments were mapped in fast total power on-the-fly mode with both polarizations of the 7-pixel low-frequency arrays (LFA) tuned to the carbon fine-structure line [C II] $^3P_{3/2} - ^3P_{1/2}$ 158 μm ($f_0 = 1900.53690$ GHz; Cooksy et al. 1986). The three mapped fields were over-sampled at 3'' spacing, with 0.2 sec integration time per dump. The high-frequency array (HFA), tuned to the [O I] $^3P_1 - ^3P_0$ 63 μm ($f_0 = 4744.77749$ GHz; Zink et al. 1991) transition, was operated in parallel, but post-flight analysis revealed a too weak line intensity for quantitative analysis. Therefore, we decided to revisit the three strongest [C II] condensations, in each filament, with targeted, deep(er) integrations in rather slow chopped mode (rate 0.626 Hz) for better stability. For these observations the LFA was operated in split mode, with the LFA-V tuned to [O I] $^3P_0 - ^3P_1$ 145 μm ($f_0 = 2060.06886$ GHz), while the LFA-H was still recording [C II]. The HFA was running in parallel, but due to the frequency dependent array geometry, only the central pixels of the two arrays were co-aligned on the sky.

Half-power main beam sizes (θ_{mb} : 14''1 for [C II], 13'' for [O I] 145 μm and 6''3 for [O I] 63 μm) and efficiencies ($\langle\eta_{mb}\rangle = 0.64$ for LFAV, 0.66 for LFAH, and 0.68 for HFA, respectively), derived from planet observations, were provided by the GREAT consortium. The instrument parameters are described in Risacher et al. (2018). Both spectrometer arrays use NbN-based hot electron bolometer mixers, driven by either solid-state (LFA) or quantum cascade laser (HFA) local oscillator sources. The LFA operates 14 pixels, seven in each polarization, in a hexagonal arrangement with 31''8 radial spacing around a central pixel. The HFA has the same symmetry, using the V polarization only, with 13''8 radial spacing. Co-alignment between the central pixels is generally better than 1'' (Risacher et al., 2018). For this experiment we tracked on the central HFA pixel. Pointing was established by the telescope operators on nearby optical reference stars, to an accuracy of 1-2''. Prior to each flight series, the optical axis of the GREAT instrument had been aligned to these imagers by observations of planets. Fast Fourier Transform Spectrometers (FFTS4G, updated from (Klein et al., 2012)) offer 32k channels across the 0–4 GHz intermediate-frequency bands.

Raw data were amplitude calibrated with the kosma *kalibrate* software package (version 2022.04), following (Guan et al., 2012). The data were corrected for atmospheric extinction and calibrated in T_{mb} . The atmospheric transmission was smooth near the targets’ velocities, except for the pointed observations of [O I] 145 μm towards -G3 (in April 2022) that were made impossible because of strong blending with a prominent telluric ozone feature.

Further processing of the calibrated data was performed with the GILDAS software². An initial inspection of the data cube was done in order to identify and eliminate unusable spectra with artefacts. Spectra with baseline ripples were identified by comparing the baseline noise with the radiometric noise deduced from the calibration and discarded. Once in main beam tempera-

¹ The German REceiver for Astronomy at Terahertz frequencies (up-GREAT) is a development by the MPI für Radioastronomie and the KOSMA/Universität zu Köln, in cooperation with the DLR Institut für Optische Sensorsysteme.

² <http://www.iram.fr/IRAMFR/GILDAS>

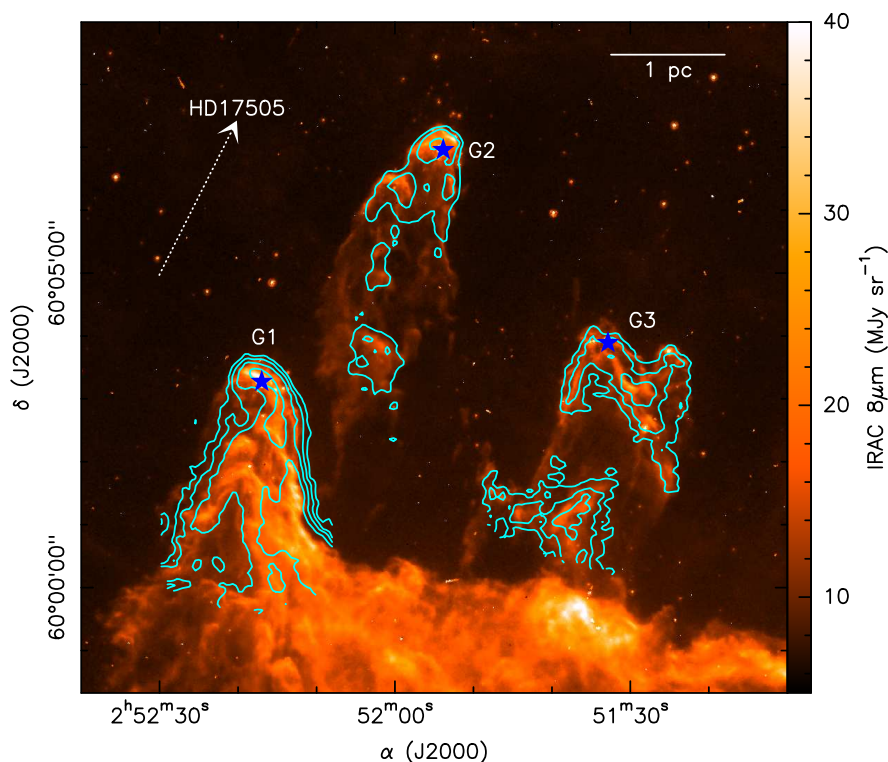


Fig. 1. *Spitzer*/IRAC $8\ \mu\text{m}$ image of the three filaments in IC 1848 (G1–G3, left-to-right, respectively). Bright IRAC compact sources are clearly visible at the head of the filaments (white saturated spots in the image). Cyan contours show the [C II] $158\ \mu\text{m}$ integrated line intensity observed with SOFIA/upGREAT. Contour levels are 8, 12, 18 and $27\ \text{K km s}^{-1}$, and typical 1σ noise levels are 3.3, 1.8, and $2.4\ \text{K km s}^{-1}$ in G1–G3, respectively. Blue stars mark the location of the three brightest 2MASS/WISE sources at the heads of the filaments and the white arrow shows the direction toward the O6V ionizing star HD17505.

ture, the spectra were smoothed to a resolution between 0.1 and $0.15\ \text{km s}^{-1}$ and baselines of orders one or two were removed.

3. Results and discussion

3.1. Morphology and kinematics

Figure 1 shows excellent correlation between the IRAC $8\ \mu\text{m}$ continuum emission in IC 1848 (color image), likely dominated by the PAH emission, and the [C II] line emission (cyan contours). Bright IRAC point sources are located at the head of each pillar, which coincide with 2MASS point sources classified as YSO or YSO Candidate. Their 2MASS and WISE magnitudes are listed in Table 1. From their WISE colors (Koenig & Leisawitz, 2014; Kang et al., 2017) the sources at the head of the G1 and G2 filaments can be identified as Class I, while that at the head of the G3 filament is at the boundary between Class I and Class II.

To estimate bolometric luminosities of the embedded stars from their 2MASS magnitudes, we use eq. (5) of González Hernández & Bonifacio (2009). We use the K_S magnitudes, which are least affected by extinction, and adopt the Vega K magnitude and absolute integrated flux from Table 3 of González Hernández & Bonifacio (2009). The resulting bolometric luminosities are 0.3 – $0.9\ L_{\odot}$ (Table 1). These values are not corrected for extinction.

Figure 2, top panel, shows the morphology of the [C II] line emission toward the brightest G1 filament. A bright, narrow ridge of emission is seen on the west side of the filament, with weaker emission extending toward the east. Example [C II] spectra toward selected positions marked A–F are shown on the top-right. With the exception of the position F at the base of the filament, which shows a broad line with two velocity components, the remaining spectra show consistent velocities, with the head of the filament (position A) displaying slightly redshifted emission compared to the other positions, possibly owing to the

radiation pressure exerted by the impinging UV photons or the rocket effect of the evaporating gas (Bertoldi & McKee, 1990), which causes the cloud to be accelerated away from the ionizing star. Bertoldi & McKee (1990) estimates the characteristic rocket velocity as 10 – $5\ \text{km s}^{-1}$. This is higher than the $\approx 1\ \text{km s}^{-1}$ velocity difference between the surface and the center of the G1 filament (Figure 2, lower-left), possibly due to projection effects. The [O I] velocities at the head of the G1 filament are consistent with [C II] (Figure A.6, positions G, H).

To investigate further the kinematics of the gas across the filament, we have computed the first and second moment maps of the [C II] line emission. The bottom-left panel shows the mean [C II] velocity computed as $\bar{v} = \sum v_i T_i / \sum T_i$, and the bottom-right panel shows the velocity dispersion, $\sigma_v = \sqrt{v^2 - \bar{v}^2}$. The mean line velocity increases by up to $\approx 1\ \text{km s}^{-1}$ at the head and near the edges compared to the center of the filament, while the velocity dispersion remains uniform within the observational uncertainties. A hint of this velocity shift can also be seen in the position A spectrum in Figure 2. The base of the G1 filament is characterized by a significantly lower mean velocity and higher velocity dispersion, owing to the presence of a distinct velocity component at $-40\ \text{km s}^{-1}$ (Figure 2, position F), which is likely a part of the extended molecular shell that can be seen in the IRAC image (Figure 1). Outside of this region, the velocity dispersion is quite uniform along the filament, in contrast to Pillar 2 in M16, where the dispersion increases toward the tail (see Fig. 8 of Karim et al. 2023). This is likely due to the difference in the UV illumination between the two regions. The three M16 pillars are illuminated by a handful of bright O5–7 stars located at a $\sim 3\ \text{pc}$ projected distance (Hillenbrand et al., 1993). Karim et al. (2023) estimated the FUV field strength toward the M16 pillars is in the range 1500 – 2500 Habing units. Consequently, the UV photons have smaller influence on the kinematics of the gas and the resulting degree of turbulence in IC 1848 compared to M16.

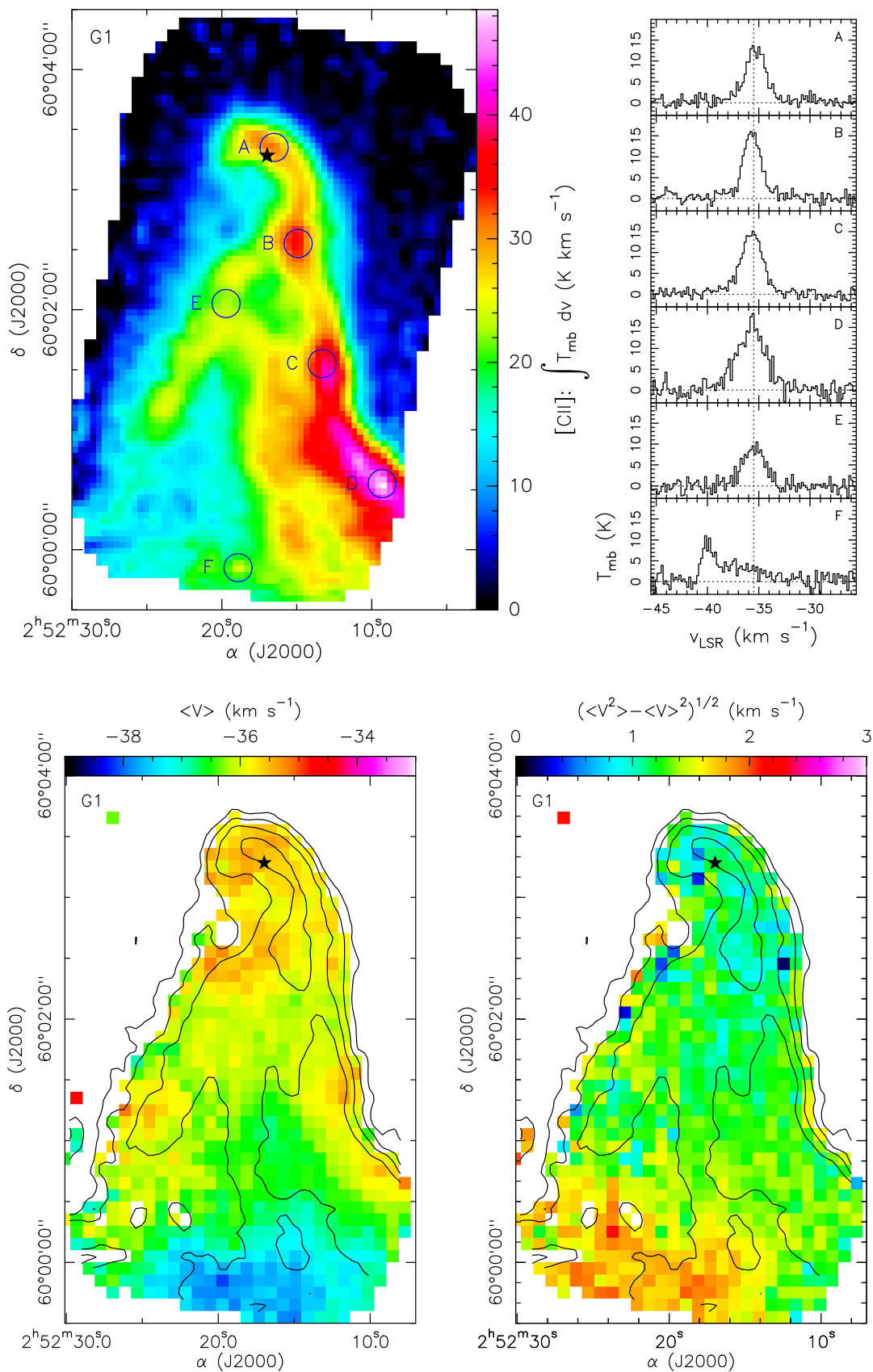


Fig. 2. (Top) Color image of the [C II] integrated line intensity in the -40 to -33.5 km s⁻¹ velocity range toward the G1 filament. The right panel shows spectra at selected positions labeled A–F in the image. Blue circles correspond to the FWHM SOFIA beam size at the [C II] frequency. (Bottom) Maps of the [C II] line center velocity and velocity dispersion toward the G1 filament (color images, left and right panels, respectively). Only pixels with [C II] intensities above 3.5σ (11.6 K km s⁻¹) are shown. Black contours show the integrated line intensity, with the same contour levels as in Figure 1. Black stars mark the location of the bright IRAC compact source.

Table 1. WISE and 2MASS Magnitudes of the Point Sources at the Heads of the G1–G3 Filaments.-

<i>Pillar</i>	<i>2MASS Source</i>	<i>J</i>	<i>H</i>	<i>K_S</i>	<i>w1</i>	<i>w2</i>	<i>w3</i>	<i>w2 – w3</i>	<i>w1 – w2</i>	<i>Class</i>	<i>L_{bol}</i>
G1	J02521697+6003170	16.498	14.94	14.546	10.895	8.659	4.961	3.698	2.236	I	0.37
G2	J02515380+6006581	15.934	13.625	11.776	8.883	7.018	4.889	2.129	1.865	I	0.81
G3	J02513283+6003542	13.005	11.523	10.447	9.261	8.112	5.562	2.550	1.149	I/II	0.86

Note: Entries in the table are: 2MASS source identifier, 2MASS J, H, and K_S magnitudes (1.235, 1.662, and 2.159 μm), WISE $w1 - w3$ magnitudes (3.4, 4.6, and 12 μm), WISE colors, the resulting classification (Koenig & Leisawitz, 2014; Kang et al., 2017), and an estimate of the bolometric luminosity (in solar luminosities) based on the K_S magnitude (González Hernández & Bonifacio, 2009). We assume a distance of 1.9 kpc corresponding to the distance modulus of 11.39 mag, a Vega K_S -band magnitude of 0.043 and a flux of $1.1 \times 10^{-7} \text{ erg s}^{-1} \text{ cm}^{-2}$ (Table 3 of González Hernández & Bonifacio 2009).

Table 2. Molecular Hydrogen and [CII] Column Densities.

Position	($\Delta\alpha, \Delta\delta$)	T_d	τ_{350}	β	$N(\text{H}_2)$	A_V	[C II]	$N(\text{C}^+)$
	($''$)	(K)			(cm^{-2})		(K km s^{-1})	(cm^{-2})
G1 A	(-5.1, 3.8)	34.7	1.1×10^{-3}	0.00	–	–	24.3	
G1 B	(-17.1, -44.2)	28.5	8.3×10^{-4}	0.69	1.00×10^{22}	9.1	28.4	3.3×10^{17}
G1 C	(-29.1, -104.2)	29.4	3.4×10^{-4}	0.89	4.16×10^{21}	3.8	32.2	3.8×10^{17}
G1 D	(-59.1, -164.2)	27.3	3.6×10^{-4}	1.07	4.34×10^{21}	3.9	39.2	4.6×10^{17}
G1 E	(18.9, -74.2)	27.9	1.0×10^{-4}	0.55	1.23×10^{21}	11.1	20.3	2.4×10^{17}
G1 F	(12.9, -206.2)	28.0	3.6×10^{-4}	0.85	4.34×10^{21}	3.9	18.5	2.2×10^{17}
G2 A	(3.5, 7.3)	32.5	9.6×10^{-4}	0.36	1.16×10^{22}	10.5	15.5	1.8×10^{17}
G2 B	(39.5, -34.7)	30.1	6.1×10^{-4}	0.23	7.35×10^{21}	6.6	13.1	1.5×10^{17}
G2 C	(-8.5, -34.7)	26.0	4.1×10^{-4}	0.90	4.90×10^{21}	4.4	10.2	1.2×10^{17}
G2 D	(63.5, -112.7)	24.7	2.7×10^{-4}	0.72	3.25×10^{21}	2.9	8.3	1.0×10^{17}
G2 E	(63.5, -190.7)	26.3	2.4×10^{-4}	0.67	2.89×10^{21}	2.6	11.0	1.3×10^{17}
G3 A	(-2.9, -13.6)	28.8	7.0×10^{-4}	0.51	8.43×10^{21}	7.6	15.3	1.8×10^{17}
G3 B	(-32.9, -43.6)	27.6	4.7×10^{-4}	0.80	5.70×10^{21}	5.2	19.2	2.2×10^{17}
G3 C	(33.1, -49.6)	27.9	2.9×10^{-4}	0.76	3.50×10^{21}	3.2	10.3	1.2×10^{17}
G3 D	(-56.9, -115.6)	29.7	2.1×10^{-4}	0.57	2.55×10^{21}	2.3	8.6	1.0×10^{17}
G3 E	(39.1, -169.6)	29.2	2.3×10^{-4}	0.80	2.81×10^{21}	2.5	18.0	2.1×10^{17}

Note: Entries in the table are: position (see Figure 2, top panel), offsets from the image center, best fit dust temperature, 350 μm optical depth, grain emissivity exponent, H_2 column density in the $36''7$ SPIRE beam at 500 μm and the corresponding visual extinction, [C II] integrated line intensity in a $36''7$ beam, and the corresponding C^+ column density. Image center positions (J2000) are: (02:52:17.19, +60:03:17.22) for G1, (02:51:53.91, +60:06:56.97) for G2, and (02:51:32.90, +60:03:53.34) for G3.

Moment maps of the G2 and G3 filaments are shown in Figures A.1–A.2 in the Appendix. Filament G2 shows an elliptical morphology, with the west side (Figure A.1, positions A and C) significantly redshifted compared to the east side (positions B, D, and E). There is some evidence for lower velocity dispersions on the west side, but the uncertainties are large. Filament G3 splits into two distinct parts, the head and the base, which display large differences in the mean velocity and velocity dispersion (Figure A.2 in the Appendix). The [C II] spectrum at the base is double peaked, indicating the presence of a separate velocity component at about -43 km s^{-1} .

The kinematic structure of the three filaments is further displayed in the velocity channel maps (Figures A.3–A.5 in the Appendix, filaments G1–G3, respectively). Based on the morphology of the $\text{H}\alpha$ emission, Thompson et al. (2004) argued that although the three clouds lie close together on the sky, this arrangement may be a chance superposition, with G1 located behind the illuminating star and G2/G3 in front. Such a geometry could explain the $\sim 5 \text{ km s}^{-1}$ velocity differences between G1 and the other two clouds. However, the observed velocity gradients observed along all three filaments, with the [C II] emission

at the head being redshifted with respect to the tail, would seem to indicate that the filaments are collocated on the front side of the illuminating star (see, e.g., Bertoldi & McKee 1990; Pound 1998). As discussed in Sect. 3.4, the observed [C II]/[O I] $63 \mu\text{m}$ line intensity ratio does not seem consistent with back-side illuminated PDR models of G2 and G3. The exact geometry of the three filaments with respect to the illuminating star remains, therefore, ill-defined.

3.2. Hydrogen column densities

In addition to the SOFIA and *Spitzer* data, far-infrared continuum images of IC 1848, obtained using PACS and SPIRE instruments, are available in the *Herschel* Science Archive, which allow characterization of the continuum spectral energy distribution (SED) over a broad wavelength range to constrain the dust temperature and the H_2 column density required for the PDR modeling (Sec. 3.4). Figure 3 shows the continuum SEDs at positions A–F in the G1 filament. All continuum images have been convolved to the $36''7$ resolution (full width at half maxi-

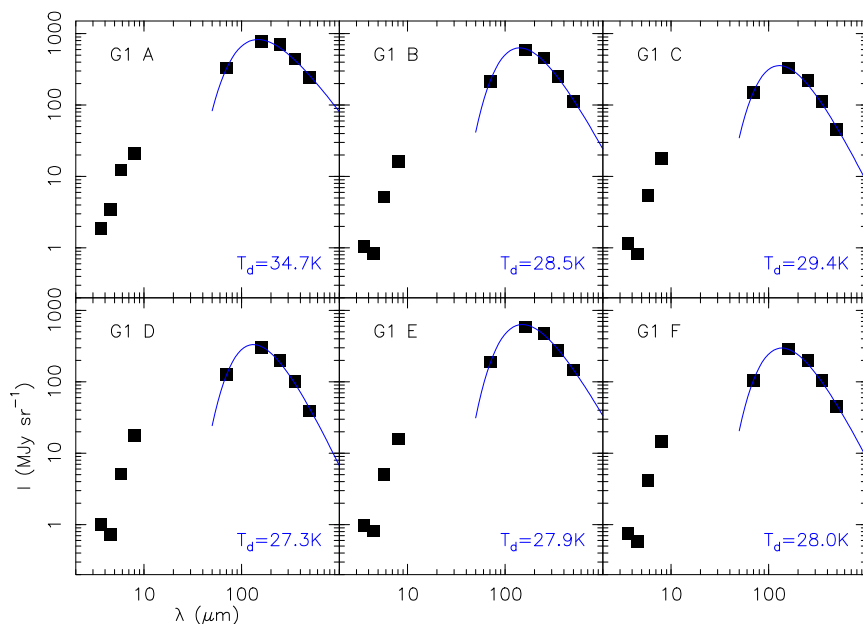


Fig. 3. Spectral energy distributions toward positions A–F in the G1 filament based on *Spitzer* and *Herschel* observations. Blue curves show the modified blackbody fits to the *Herschel* PACS and SPIRE fluxes from which the dust temperatures and 350 μm optical depths used for the column density determination are derived. Typical flux calibration uncertainties are $\sim 5\%$.

num, FWHM) of the longest-wavelength 500 μm SPIRE channel. Blue curves show single-component modified blackbody fits, $I_\nu = B_\nu(T_d) \times [1 - \exp(-\tau_{350} \times (350\mu\text{m}/\lambda)^\beta)]$, to the PACS and SPIRE data only. Best fit parameters, the dust temperature (T_d), the 350 μm optical depth (τ_{350}), and the grain emissivity exponent (β) are listed in Table 2.

The SED toward position A is well described by a scaled blackbody ($\beta = 0$). This is consistent with the flux, even at the longest SPIRE wavelengths, being dominated by the stellar source seen in the IRAC images rather than dust emission. The remaining positions have steeper dust emission spectra characterized by average dust temperatures of ~ 28 K, low 350 μm optical depths, and shallow values of $\beta \sim 0.8$.

The H_2 column densities in a $36''.7$ beam are computed using the formula $N(\text{H}_2) = 2a\rho R_{gd}/3m_{\text{H}} \times \tau_{350}/Q_{350}$ (Lis & Goldsmith, 1990), where $a = 0.1 \mu\text{m}$ is the mean grain radius, $\rho = 3 \text{ g cm}^{-3}$ is the mean density, $R_{gd} = 100$ is the gas-to-dust mass ratio, m_{H} is the hydrogen mass, and Q_{350} is the 350 μm grain emissivity coefficient. Extrapolating the 125 μm grain emissivity coefficient of Hildebrand (1983) (7.5×10^{-4}) with a ν^2 frequency dependence gives $Q_{350} = 1 \times 10^{-4}$, corresponding to the grain mass opacity coefficient $\kappa_{350} = 3Q/4/a/\rho/R_{dg} = 0.025 \text{ cm}^2 \text{ g}^{-1}$, including the gas-to-dust ratio (see Lis et al. 1998). The resulting H_2 column densities are listed in Table 2 together with the corresponding visual extinction values, computed assuming the conversion factor of $N_{\text{H}} = 2.21 \times 10^{21} \text{ cm}^{-21} A_V(\text{mag})$ (Güver & Feryal, 2009). The typical visual extinction values characterizing the [C II] emitting gas are moderate, ranging from $A_V \sim 10$ near the head of the filament to ~ 4 at the base. The characteristic width of the G1 filament is $\sim 90''$, corresponding to 0.8 pc, or $2.6 \times 10^{18} \text{ cm}$ at a distance of 1.9 kpc. Assuming the same depth along the line of sight, the H_2 column densities toward the head of the filament correspond to a mean volume density of $\sim 4500 \text{ cm}^{-3}$. This should be considered a lower limit, as narrower filamentary structures can be seen in the [C II] and dust continuum images. These values are used as input for the PDR models described below.

Modified blackbody fits toward positions A–E in the G2 and G3 filaments are shown in Figure A.7 in the Appendix and best fit parameters are listed in Table 2. The dust temperatures, H_2

column densities, and the corresponding visual extinction values are comparable to those in the G1 filament. The dust temperature, A_V , and average density estimates derived here are in a reasonable agreement with those derived by Thompson et al. (2004) based on SCUBA and IRAS HIRES fluxes (see Table 5 of Thompson et al. 2004).

In addition to the H_2 column densities derived from dust SED fits, Table 2 lists the [C II] line intensities and the corresponding C^+ column densities at the same positions derived using equations (26) and (43) of Goldsmith et al. (2012). PDR models (Figure 6) suggest that the [C II] emission originates in the outer $A_V \sim 1.5$ molecular layer characterized by gas temperatures between ~ 50 and 160 K. Consequently, we use an average temperature of 100 K and an average H_2 density of 4500 cm^{-3} derived above in the C^+ column density calculations. Typical C^+ column densities in the G2 and G3 filaments are of order $1 - 2 \times 10^{17} \text{ cm}^{-2}$, while those in the G1 filament are a factor of ~ 2 higher (Table 2). Assuming a C^+ abundance of $\sim 2.5 \times 10^{-4}$ with respect to H_2 in the outer molecular layer, as suggested by PDR models, the [C II] emission traces on average $\sim 17\%$ of the total H_2 column density derived from the dust SED fits. The C^+ column densities in IC 1848 are toward the low end of the values derived by Karim et al. (2023) in the M16 pillars, $\sim 2 \times 10^{17} - 4.7 \times 10^{18} \text{ cm}^{-2}$. This is once again likely due to the difference in the FUV illumination between the two regions.

3.3. Atomic oxygen observations

In addition to the fully-sampled [C II] maps, the 63 μm and 145 μm [O I] fine structure lines were observed at selected positions. [O I] spectra toward the G1 filament with detections above 4σ level for the integrated line intensity are shown in Figure A.6 (upper panel) in the Appendix. The 63 μm line is detected at 6 positions, labeled G–L, while the 145 μm line is detected at 3 positions, labeled M–O (see Figure A.6). The [O I] integrated line intensities are listed in Table 3, together with [C II] line intensities at the same positions extracted from the fully-sampled map.

The average [O I] 63 μm /[C II] intensity ratio (in K km s^{-1}) for positions G–L is ~ 0.10 , while the average [O I] 145 μm /[C II]

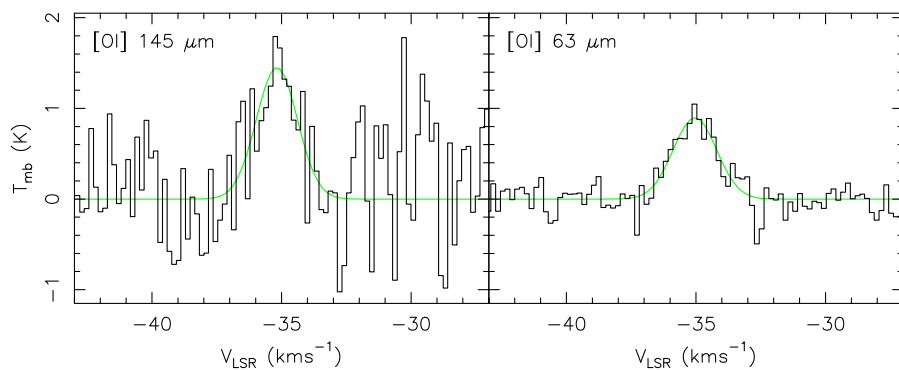


Fig. 4. Equally weighted average [O I] spectra toward the head of the G1 filament (within the white rectangle in Figure A.6). Averages include [O I] 63 μm spectra at 14 individual positions and [O I] 145 μm spectra at 3 individual positions. The excess noise on the right hand side of the [O I] 145 μm spectrum is due to increased atmospheric opacity of a nearby telluric ozone line.

Table 3. [C II] and [O I] Line Intensities at Selected Positions.

Position	($\Delta\alpha, \Delta\delta$) ($''$)	[C II] (K km s $^{-1}$)	[O I] 63 μm (K km s $^{-1}$)	[O I] 145 μm (K km s $^{-1}$)	[O I]/[C II]
G1 G	(1.0, 5.0)	29.5 ± 0.91	4.02 ± 0.43	–	0.14
G1 H	(–12.4, 5.4)	26.2 ± 0.85	2.88 ± 0.40	–	0.11
G1 I	(–20.5, –33.6)	24.1 ± 0.84	2.51 ± 0.44	–	0.10
G1 J	(–13.0, –45.0)	31.8 ± 0.77	2.91 ± 0.41	–	0.09
G1 K	(–26.4, –44.7)	20.5 ± 0.85	2.09 ± 0.39	–	0.10
G1 L	(–23.1, –56.2)	27.0 ± 0.81	2.04 ± 0.44	–	0.08
Average		26.5 ± 1.5	2.74 ± 0.30		0.10
G1 Head		19.9 ± 0.9	1.97 ± 0.13	–	0.10
G1 M	(4.6, –12.3)	13.3 ± 0.85	–	4.41 ± 0.98	0.33
G1 N	(–14.0, –21.0)	21.7 ± 0.80	–	3.62 ± 0.69	0.17
G1 O	(–30.4, –117.3)	34.2 ± 0.95	–	3.81 ± 0.93	0.11
Average		23.1 ± 6		3.95 ± 0.24	0.20
G1 Head		19.9 ± 0.9		2.93 ± 0.36	0.15
G2 F	(10.9, 4.9)	14.0 ± 1.04	1.53 ± 0.23	–	0.11
G2 G	(–2.0, 4.3)	19.4 ± 0.83	1.49 ± 0.23	–	0.08
G2 H	(4.1, 16.4)	17.7 ± 0.87	1.72 ± 0.22	–	0.10
G2 I	(33.1, –25.6)	12.9 ± 0.87	2.02 ± 0.30	–	0.16
Average		15.6 ± 1.3	1.59 ± 0.14		0.10

Note: Entries in the table are: position (see Figure A.6, left panel), offsets from the image center, the [O I] and [C II] integrated line intensities, and the corresponding [O I] to [C II] intensity ratio. [O I] line intensities are computed in the velocity range -37.2 to -32.9 km s $^{-1}$ for G1 and -44.1 to -37.9 km s $^{-1}$ for G2, corresponding to two FWHM line widths of the corresponding average [O I] 63 μm spectra. The uncertainties for the line intensities at individual positions and the average [O I] 145 μm line toward the G1 Head are computed from the spectra, while those listed for the remaining averages are uncertainties of the mean (σ/\sqrt{N}), where σ is the standard deviation of the ensemble and N is the number of measurements). Image center positions (J2000) are: (02:52:17.19, +60:03:17.22) for G1, and (02:51:53.91, +60:06:56.97) for G2.

intensity ratio for positions M–O is ~ 0.20 . This suggests that the [O I] 145 μm line is typically stronger than the 63 μm line. The [O I] 63 μm line is detected at four positions in the G2 filament (see Table 1 and Figure A.6, lower panel), and is not detected in the G3 filament. The [O I] 63 μm /[C II] intensity ratios in the G2 filament are in the same range as those observed in G1.

Given the sparse and limited spatial coverage, limited signal-to-noise ratio of the [O I] 145 μm spectra, and the difference in the beam size at the frequencies of the two oxygen lines, the [O I] 63 μm /145 μm intensity ratio cannot be determined with high accuracy. However, positions N and I are located nearby, 14'' apart along the ridge of the [C II] emission and the [O I] 63 μm /145 μm intensity ratio at these positions is ~ 0.7 . An independent estimate of the [O I] 63 μm /145 μm is obtained by

averaging [O I] spectra near the head of the G1 filament, within the white rectangle in Figure A.6. The [O I] 63 and 145 μm lines are both detected with a signal-to-noise ratio of 14 and 8, respectively. The resulting [O I] line intensities are reported in Table 3 (lines labeled “G1 Head”) together with the average [C II] integrated line intensity within the white rectangle. The [O I] 63 μm /145 μm ratio is 0.67, consistent with the values derived above, further supporting the conclusion that the [O I] 63 μm line is weaker than the 145 μm line.

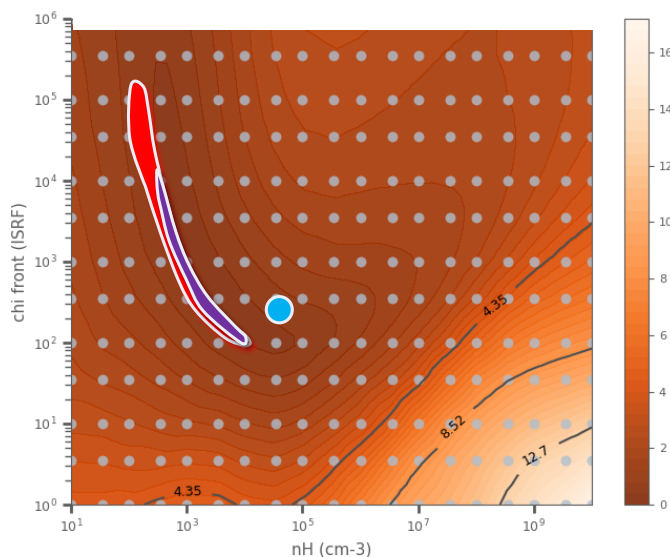


Fig. 5. χ^2 values for a grid of isochoric ISMDB models compared to the observed fine structure line intensities in the G1 filament. Blue circle and the elongated red area show best fits, respectively, to the [C II]/[O I] $145\ \mu\text{m}$ data at positions M–O and [C II]/[O I] $63\ \mu\text{m}$ data at positions G–L. The elongated magenta area shows the best fit to all data with [O I] $145\ \mu\text{m}$ line intensities scaled down by a factor of 3, as described in the text. All models assume normal incidence. Increasing the incidence angle to 60° provides comparable fit, but shifts the best-fit solution to higher densities and lower χ values (magenta area).

3.4. PDR modeling

To model the fine structure line emission in IC 1848 we use the Meudon PDR code, a publicly available, state-of-the-art astrochemistry code (Le Petit et al., 2006). Our objective is to verify whether the observed line intensities are consistent with the geometry and the UV illumination of IC1848. The Meudon code is well suited for our analysis, since it is one of very few astrochemistry codes that computes self-consistently the radiative transfer, the chemistry both in the gas phase and on grain surfaces, as well as the thermal processes and thermal balance at each point within the cloud. The code simulates a stationary plane-parallel slab of gas and dust illuminated on both sides by the radiation field from the far UV (FUV) to the radio domain. This radiation field is discretized on a wavelength grid (typically 500,000 points) and the radiative transfer equation is solved at each wavelength, and at each position in the cloud, considering (a) absorption in the continuum by the distribution of grains and by the ionization of atoms such as carbon, (b) absorption in the atomic lines of hydrogen, the Lyman and Werner transitions of H_2 as well as the pre-dissociating lines of CO isotopologues (in total more than 30,000 UV absorption lines are considered), (c) backscattering by dust, and (d) re-emission of photons as the fluorescent UV photons emitted by H and H_2 (see Goicoechea & Le Bourlot 2007).

This detailed solution of the radiative transfer equation gives the spectral energy density at all wavelengths and positions within the cloud, which is then used to compute locally precise photo-destruction rates by direct integration of the photo-absorption cross-sections (Heays et al., 2017) with the monochromatic energy density. This means that photo-destruction rates include the UV shielding of molecules by H Lyman transitions and H_2 Lyman and Werner bands. So, whereas most of other astrochemical codes rely on basic approximations (simple exponential fits) to treat absorption of UV photons, here,

thanks to the detailed treatment of the photo-destruction processes, the destruction rates of molecules are determined directly, and so their densities as a function of the position are computed more precisely.

For the chemistry, the code considers approximately 200 chemical species linked by a chemical network of ~ 2000 chemical reactions. In the gas phase, in addition to the standard exothermic reactions that constitute the bulk of chemical pathways, state-to-state reactions are considered for key endothermic reactions. For the grain surface chemistry, a power law grain size distribution is considered (Mathis et al., 1977). The temperature for grains in each size bin is computed balancing absorption and emission of photons. The processes that are considered are the adsorption from the gas, reactions in the bulk and on the surface considering thermal and tunneling effects, desorption processes (thermal and non-thermal: photo-desorption, cosmic ray desorption, chemical desorption, i.e., release of molecules into the gas phase due to the exothermicity of some reactions). The Meudon PDR code has another strong advantage over most other astrochemistry codes: it computes very precisely the formation of H_2 on dust grains. Indeed, it can either consider Langmuir-Hinshelwood and Eley-Rideal processes with the rate equation formalism (Le Bourlot et al., 2012), or even consider stochastic processes on dust (Le Petit et al., 2009; Bron et al., 2014, 2016).

3.4.1. ISMDB models

A particularly useful online tool is the InterStellar Medium DataBase³, which allows quick and easy access to pre-calculated theoretical models for various ISM conditions and objects, including models produced by the Meudon PDR code. Presently, ISMDB gives access to several thousand PDR models covering a wide range of astrophysical conditions. To prepare and interpret observations, ISMDB provides an inverse search service to allow queries on observables to find the best models that match observations and gives access to line intensity maps in a parameter space (e.g., the total hydrogen nuclei volume density $n_{\text{H}} = n(\text{H}) + 2 \times n(\text{H}_2)$, the ISRF scaling factor χ in Mathis units⁴, Mathis et al. 1983). Once the best fit model is found, model results can be downloaded without the need for running the code on a local machine.

To analyze the observed fine structure line intensities in IC1848, we use the ISMDB inverse search tool based on a grid of isochoric (constant density) models computed using the latest public version of the Meudon PDR code (1.5.4). We assume front side illumination (enhanced illumination of side of cloud facing the observer), and the total thickness of the cloud corresponding to $A_V = 10$ mag, as derived above from the SED analysis. We note that the exact value of A_V is not important for the computations, as the fine structure line emission originates from the surface of the PDR (see Figure 6 below). We have verified that models with $A_V = 5$ and 10 mag predict essentially the same line intensities. The two key parameters varied in the fit are the gas density and the radiation field scaling intensity factor, χ , with the observed fine structure line intensities being input observables. We compute averages of the individual [C II] and [O I] $63\ \mu\text{m}$ line intensities at positions G–L, and of the [C II] and [O I] $145\ \mu\text{m}$ line intensities at positions M–O and use these values as input for the ISMDB fit, assuming a 30% uncertainty as an estimate of both statistical and calibration uncertainties.

³ ISMDB; <http://ismdb.obspm.fr>

⁴ See Sect. 3.2.1 of the Meudon PDR Code Documentation; <https://data.obspm.fr/ism/files/PDRDocumentation/PDRDoc154.pdf>

Table 4. PDR Model Results.

Model	A_V	Star	D (pc)	θ (deg)	n_H (cm^{-3})	$I([\text{C II}])$ (K km s^{-1})	$I([\text{O I}] 63)$ (K km s^{-1})	$I([\text{O I}] 145)$ (K km s^{-1})	$I([\text{O I}] 63)/$ $I([\text{C II}])$	$I([\text{O I}] 145)/$ $I([\text{C II}])$
1027	10	O 5 V	-13	0	9×10^3	26.43	1.74	0.53	0.066	0.020
1028	10	O 5 V	13	0	9×10^3	20.51	0.50	0.53	0.025	0.026
1029	10	O 5 V	-15	30	9×10^3	26.04	1.33	0.40	0.051	0.015
1030	10	O 5 V	15	30	9×10^3	19.84	0.37	0.40	0.018	0.020
1031	10	O 5 V	-26	60	9×10^3	21.88	0.41	0.11	0.019	0.005
1032	10	O 5 V	26	60	9×10^3	15.81	0.10	0.11	0.006	0.007
1033	10	O 5 V	-15	30	4.5×10^4	22.48	2.35	0.69	0.105	0.031
1034	10	O 5 V	15	30	4.5×10^4	20.85	1.42	0.69	0.068	0.033
Observed	-	-	-	-	-	13–32	1.4–4.0	3.6–4.4	0.08–0.14	0.11–0.33

Note: Entries in the table are: model number, stellar type, distance (pc; negative and positive values imply front-side and back-side illumination, respectively), the [O I] 63 μm , [O I] 145 μm , and [C II] integrated line intensities (K km s^{-1}), the [O I] 63 [C II] line ratio, and the [O I]/145 μm to [C II] line ratio. All models assume a turbulent velocity dispersion of 0.9 km s^{-1} , as suggested by the observed [C II] line widths and face-on illumination.

The χ^2 for the ISMDB fit to the combined data set (Figure 5; color map and thin black contours) shows a broad, shallow distribution with no unique solution. Since we do not have observations of the two [O I] fine structure lines at the same positions, we then fit separately the combinations of [C II]/[O I] 63 μm at positions G–L and [C II]/[O I] 145 μm at positions M–O. A fit to the observed [C II] and [O I] 145 μm line intensities at positions M–O gives a unique solution with $n_H \approx 3 \times 10^4 \text{ cm}^{-3}$ and $\chi \approx 200 - 250$ (blue dot), while the observed [C II] and [O I] 63 μm line intensities at positions G–L are consistent with a range of parameters within the elongated red area. The two regions do not overlap; there is no unique solution that is consistent with both data sets. The [O I] 145 μm observations suggest higher gas densities compared to the [O I] 63 μm observations. For $\chi = 200 - 250$, the best fit for positions G–L has a density $n_H \approx 1 - 3 \times 10^3 \text{ cm}^{-3}$, an order of magnitude lower than the value derived from the [O I] 145 μm fit. These results show that the observed [O I] 63 μm /145 μm ratio cannot be explained easily with the PDR models. To bring the two solutions into agreement, we must lower the [O I] 145 μm line intensity by about a factor of 3. The best fit to the combined data set with such scaling is shown as the narrow magenta elongated area. We note that the mean gas density $n_H \approx 9 \times 10^3 \text{ cm}^{-3}$ derived from the dust SED analysis is consistent with the southern tip of the best fit area; the corresponding χ value is ≈ 100 .

The observed PACS fluxes toward the IC 1848 filaments allow an independent estimate of the UV radiation field strength (Kramer et al., 2008; Roccatagliata et al., 2013). We consider as an example position B near the head of the G1 filament, but away from the embedded IRAC point source. The PACS 70 and 160 μm fluxes at this position are 212 and 598 MJy sr^{-1} , respectively (Fig. 3). The corresponding effective filter widths read from the filter curves in the PACS online documentation are $\sim 1.3 \times 10^{12}$ and 1.1×10^{12} Hz, respectively. The UV field strength can then be estimated using eq. (2) of Roccatagliata et al. (2013) by adding the 70 and 160 μm PACS intensities (Schneider et al., 2016). The resulting value is $\chi = 74$ Habing units, corresponding to 96 Mathis units, consistent with the southern tip of the elongated best fit area in Figure 5.

3.4.2. PDR models illuminated by a star

The ISMDB models discussed above assume isotropic radiation and a normal incidence angle. To investigate the model results in more detail, we ran a series of offline PDR models with different geometries. The results are summarized in Table 4. The input parameters include the spectral type of the illuminating star (O5V is the closest spectral type considered in the Meudon code), distance D (negative values imply front-side illumination and positive values back-side illumination), inclination angle θ , A_V , and gas density n_H . The UV radiation field of an O5V star at a distance of 13 pc corresponds to $\chi \sim 35$ Mathis units (F. Le Petit, private comm.), lower than the values derived above. We note, however, that using a stellar spectral type as input parameter for the Meudon PDR code is different from using an ISRF scaling factor χ in the ISMDB analysis. χ is a scaling factor for an isotropic ISRF, whereas the radiation field from a star is plane-parallel. A plane-parallel (stellar) UV radiation field penetrates deeper into the cloud than an isotropic radiation field, resulting in higher intensities of FIR fine structure lines. The difference in the predicted line intensities can sometimes be significant.

Table 4 shows predicted fine structure line intensities and line ratios for several PDR models with different parameters computed using an off-line version of the Meudon PDR code (1.5.4). Models 1027–1028 correspond to normal incidence at the closest possible (projected) distance from the illuminating star (highest possible illumination). Models 1029–1030 correspond to more physical geometries, with inclination angles $\theta = 30$ and 60° , and the distance increased accordingly as the projected distance divided by $\sin \theta$. Models 1027 and 1029 are consistent with the observed line intensities of the [C II] and [O I] 63 μm lines, assuming front side illumination, although the [O I] 63 μm /[C II] line ratio is slightly lower than the observed values. However, the [O I] 145 μm /[C II] line ratio for all models is an order of magnitude lower than the observed values, as suggested earlier by the ISMDB models.

While models with back-side illumination produce [O I] 63/145 μm line ratios below unity, which is explained by foreground absorption of the optically thick [O I] 63 μm line (Goldsmith et al., 2021), the predicted intensities of both lines are much too low compared to [C II]. Therefore, we do not consider back-side illumination and optically thick [O I] 63 μm emission as a viable solution for the IC1848 pillars.

Since under most conditions encountered here, the [O I] 145 μm line has a higher critical density than do the [C II] and [O I] 63 μm lines, we considered two additional models (1033–1034) with the same geometry as models 1029–1030, but with density increased by a factor of 5. While the intensity of the [O I] 145 μm line increases by a factor of 1.7, it is still well outside of the observed range. The [O I] lines in IC1848 are weak and the S/N in the observed spectra is limited. Moreover, the [O I] 145 μm line is close to a telluric ozone line, which affects the calibration of the data. However, we conclude that the apparent discrepancy between the intensities of the two [O I] lines cannot be explained by instrumental effects.

Based on past experience (Joblin et al. , 2018; Wu et al. , 2018), the Meudon PDR code may underestimate the [C II] line intensity in astronomical sources. This is explained by [C II] contributions from gas in front or behind the PDR – the model only reproduces the emission associated with the PDR. For oxygen lines, the plane-parallel geometry of the code can sometimes lead to problems, because photons from optically thick lines are artificially trapped in the model, whereas in reality they can escape in directions perpendicular to the line of sight. This line trapping effect is more important for the optically thick 63 μm line, with the optically thin 145 μm line being little affected, and can artificially decrease the [O I] 63/145 μm line ratio. When comparing PDR models to observations, a scaling factor, κ , is sometime used to take into account that (a) several PDR layers along the line of sight can be present within the beam ($\kappa > 1$), (b) the PDR is inclined ($\kappa > 1$, an effect that we attempted to include directly in the analysis presented here), and (c) the PDR emission does not fill the beam ($\kappa < 1$). While the [C II] emission in IC1848 is spatially extended, beam filling factors for different tracers may vary. Since we have only sparse single-point observations of the [O I] lines with a limited S/N, we cannot ascertain the extent of the [O I] emission, which is typically less extended than [C II] given its higher critical density.

Röllig et al. (2007) presented a comparison of numerical codes developed for modeling the physics and chemistry of UV illuminated regions. Their Figure 15 shows the surface brightness of the main fine-structure cooling lines computed using eight such models. With the exception of the Meijerink code, all models give the [O I] 63/145 μm intensity ratio greater than unity (in main beam brightness temperature units). The [O I] 63/145 μm ratio predicted by the Meudon PDR code is higher compared to other codes (e.g., a factor of ~ 1.8 higher than the KOSMA- τ model prediction). The particular model used for this comparison has a high UV illumination ($\chi = 10^5$) and the results may not be representative for all physical conditions. However, the differences among predictions of the various PDR models do not appear to be large enough to account for the discrepancy in the [O I] 63/145 μm intensity ratio between the model predictions and our IC1848 observations. Given the modeling and observational uncertainties (limited S/N, calibration uncertainty), a factor 2 – 3 agreement with the observations is usually considered satisfactory. However, our observations suggest that the [O I] 63/145 μm intensity ratio is a sensitive probe of the physical conditions (density or pressure, χ) and chemistry in moderate A_V and UV illumination regions such as IC1848.

Figure 6 shows the gas temperature, density and abundance profiles near the cloud surface for Model 1027. PDR chemistry computations show that ionized carbon is only abundant in the outer $A_V \sim 1.5$ layer, transitioning to neutral carbon, CO, and other carbon-bearing species in deeper layers. Atomic oxygen extends somewhat deeper into the cloud up to $A_V \sim 2.5$, before being transformed into CO, water, and other oxygen-bearing

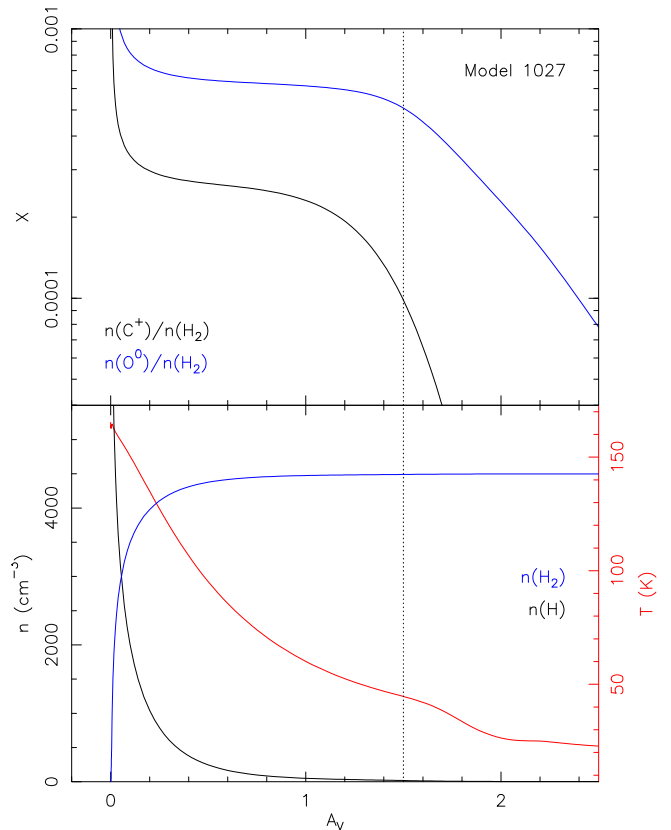


Fig. 6. Temperature, density, and abundance profiles in the outer PDR layers of Model 1027.

species. The gas in the [C II] emitting region is molecular, with temperatures between 50 and 150 K.

4. Summary and conclusions

Using the upGREAT instrument on SOFIA, we have imaged the [C II] 158 μm fine structure line in the bright-rimmed clouds G1–G3 in IC1848 and obtained pointed observations of the [O I] 63 and 145 μm fine structure lines at several positions to characterize the morphology, velocity field, and the physical conditions in the region. The fine structure line intensities are analyzed using the Meudon PDR code. The main results of this study can be summarized as follows:

1. Velocity-resolved [C II] spectra show evidence of a velocity shift at the head of the brightest G1 filament, possibly caused by radiation pressure from the impinging UV photons.
2. Archival *Herschel* PACS and SPIRE images imply H_2 column densities in the range $10^{21} - 10^{22} \text{ cm}^{-2}$, corresponding to maximum visual extinction $A_V \approx 10$. Assuming that the line-of-sight depth of the filaments is the same as their characteristic width in the plane of the sky, the average H_2 volume density is $\approx 4500 \text{ cm}^{-3}$.
3. The [C II] emission traces $\sim 17\%$ of the H_2 column density derived from the dust SED fits.
4. The [O I] 63 and 145 μm emission is generally weak in this low- χ PDR. The 63 μm line is detected above 4σ level at 6 positions in G1 and 4 positions in G2, while the 145 μm line is detected only at 3 positions in G1. Both lines are detected

at a high S/N in average spectra toward the head of the G1 filament (Figure 4), implying a low average [O I] 63/145 μm line intensity (in K km s^{-1}) ratio of ~ 0.67 .

5. PDR models are unable to explain the observed line intensities of the two [O I] fine structure lines in the IC1848 region. To obtain a good solution, the intensity of the [O I] 145 μm line would have to be a factor of 3 lower compared to the observations. The [O I] lines in IC1848 are weak and the S/N in the observed spectra is limited. However, the discrepancy between the intensities of the two [O I] lines is not likely caused by instrumental/calibration effects.

The apparent discrepancy between the model intensities of the two [O I] lines and IC1848 observations may be due to the limited signal-to-noise ratio or trapping of the [O I] 63 μm photons in a plane-parallel geometry model. Nevertheless, our observations suggest that the [O I] 63/145 μm intensity ratio is a sensitive probe of the physical conditions (density or pressure, χ) and chemistry in moderate A_V and UV illumination regions such as IC1848. Antarctic balloons are the only current FIR facilities that would allow extending this work to other sources. However, some of the future FIR Astrophysics Probe concepts include high-resolution spectroscopic capabilities in this wavelength range.

Acknowledgements. Based on observations made with the NASA/DLR Stratospheric Observatory for Infrared Astronomy (SOFIA). SOFIA was jointly operated by the Universities Space Research Association, Inc. (USRA), under NASA contract NAS2-97001, and the Deutsches SOFIA Institut (DSI) under DLR contract 50 OK 0901 to the University of Stuttgart. GREAT was a development of the MPI für Radioastronomie and the KOSMA/Universität zu Köln, in cooperation with the DLR Institut für Optische Sensorsysteme, financed by the participating institutes, by the German Aerospace Center (DLR) under grants 50 OK 1102, 1103 and 1104, and within the Collaborative Research Centre 956, funded by the Deutsche Forschungsgemeinschaft (DFG). Part of this research was carried out at the Jet Propulsion Laboratory, California Institute of Technology, under a contract with the National Aeronautics and Space Administration (80NM0018D0004). D.C.L., P.F.G., and Y.S. acknowledge financial support from the National Aeronautics and Space Administration (NASA) Astrophysics Data Analysis Program (ADAP). We thank Franck Le Petit and William D. Langer and an anonymous referee for helpful comments.

References

Berné, O., Habart, É., Peeters, E., et al. 2022, *PASP*, 134, 054301
 Berné, O., Habart, É., Peeters, E., et al. *Science*, 383, 6686, p988,
 Bertoldi, F., & McKee, C. F. 1990, *ApJ*, 354, 529
 Bron E., Le Bourlot J., Le Petit F. 2014, *A&A*, 569, 100
 Bron E., Le Petit F., & Le Bourlot J. 2016, *A&A*, 588, 27
 Wu, R., Bron, E., Onaka, T., et al. 2018, *A&A*, 618, 53
 Chauhan, N., Ogura, K., Pandey, A. K., et al. 2011, *PASJ*, 63, 795
 Cooksy, A. L., Saykally, R. J., Brown, J. M., et al. 1986, *ApJ*, 309, 828
 Ferland, G. J., Chatzikos, M., Guzmán, F., et al. 2017, *RMxAA*, 53, 385
 Getman, K. V., Feigelson, E. D., Sicilia-Aguilar, A., et al. 2012, *MNRAS*, 426, 2917
 Goicoechea, J., & Le Bourlot, J. 2007, *A&A*, 467, 1
 Goldsmith, P. F., Langer, W. D., Pineda, J., et al. 2012, *ApJ*, 203, 13
 Goldsmith, P. F., Langer, W. D., Seo, Y., et al. 2021, *ApJ*, 916, 6
 González Hernández, J. I., & Bonifacio, P. 2009, *A&A*, 497, 497
 Guan, X., Stutzki, J., Graf, U. U., et al. 2012, *A&A* 542, L4
 Güver, T., & Özel, F. 2009, *MNRAS*, 400, 2050
 Heays A., Bosman A., & van Dishoeck E. 2017, *A&A*, 602, 105

Hester, J. J., Scowen, P. A., Sankrit, R., et al. 1996, *AJ*, 111, 2349
 Hildebrand, R.H. 1983, *QJRAS*, 24 267
 Hillenbrand, L. A., Massey, P., Strom, S. E., & Merrill, K. M. 1993, *AJ*, 106, 1906
 Ishida, K. 1970, *PASP*, 22, 277
 Joblin, C., Bron, E., Pinto, C., et al. 2018, *A&A*, 615, 129
 Kang, S.-J., Kerton, C. R., Choi, M., et al. 2017, *ApJ*, 845, 21
 Karim, R. L., Pound, M. W., Tielens, A. G. G. M., et al. 2023, *AJ*, 166, 240
 Klein, B., Hochgürtel, S., Krämer, I., Bell, et al., 2012, *A&A* 542, L3
 Koenig, X. P., & Leisawitz, D. T. 2014, *ApJ*. 791. 131
 Kramer, C., Cubick, M., Röllig, et al. 2008, *A&A*, 477, 547
 Le Bourlot J., Le Petit, F., Pinto, C., et al. 2012, 541, 76
 Le Petit, F., Nehmé, C., Le Bourlot, J., 2006, *ApJS*, 164, 506
 Le Petit, F., Barzel, B., Biham, O., et al. 2009, *A&A*, 505, 1153
 Lis, D.C., & Goldsmith, P.F. 1990, *ApJ*, 356, 195
 Lis, D.C., Serabyn, E., Keene, J., et al. 1998, *ApJ*, 509, 299
 Mackey, J., & Lim, J. 2010, *MNRAS*, 403, 714
 Mackey, J., & Lim, J. 2011, *MNRAS*, 412, 2079
 Maíz Apellániz, J., Barbá, R. H., Fernández Aranda, R., et al. 2022, *A&A*, 657, 131
 Mathis, J.S., Ruml, W., & Nordsieck, K. H. 1977, *ApJ*, 217, 425
 Mathis, J. S., Mezger, P. G., & Panagia, N. 1983, *A&A*, 128, 212
 Motte, F., André, P., & Neri, R. 1998, *A&A*, 336, 150
 Pattle, K., Ward-Thompson, D., Hasegawa, T., et al. 2018, *ApJ*, 860, L6
 Peeters, E., Habart, É., Berné, O., et al. 2024, *A&A*, 685, A74
 Pound, M.W. 1998, *ApJ*, 493, L113
 Risacher, C., Güsten, R., Stutzki, J., et al. 2018, *Journal of Astronomical Instrumentation* 7, 1840014
 Roccatagliata, V., Preibisch, T., Ratzka, T., et al. 2013, *A&A*, 554, A6
 Röllig, M., Abel, N. P., Bell, T., et al. 2007, *A&A*, 467, 187
 Schneider, N., Bontemps, S., Motte, F., et al. 2020, *A&A*, 591, A40
 Schneider, N., Simon, R., Guevera, C., et al. 2020, *PASP*, 132, 104301
 Schneider, N., Bonne, L., Bontemps, S., et al. 2023, *NatAs*, 7, 546
 Thompson, M. A., White, G. J., Morgan, L. K., et al. 2004, *A&A*, 414, 1017
 Tiwari, M., Wolfire, M., Pound, M. W., et al. 2022, *ApJ*, 164, 150
 Williams, R.J.R. 2007, *ApSpSc*, 307, 179
 Young, E. T., Becklin, E. E., Marcum, P.M., et al. 2012, *ApJ*, 749, L17
 Zink, L.R., Evenson, K. M., Matsusima, F., et al. 1991, *ApJL*, 371, L85

Appendix A:

Figures [A.1](#) and [A.2](#) show moment maps and [C II] spectra at selected positions toward the G2 and G3 filaments, respectively. Figures [A.3–A.5](#) show the channel maps of the [C II] emission in the filaments G1–G3, respectively. Figure [A.6](#) shows [O I] spectra toward the G1 and G2 filaments. Figure [A.7](#) shows the continuum SEDs at selected positions toward the G2 and G3 filaments.

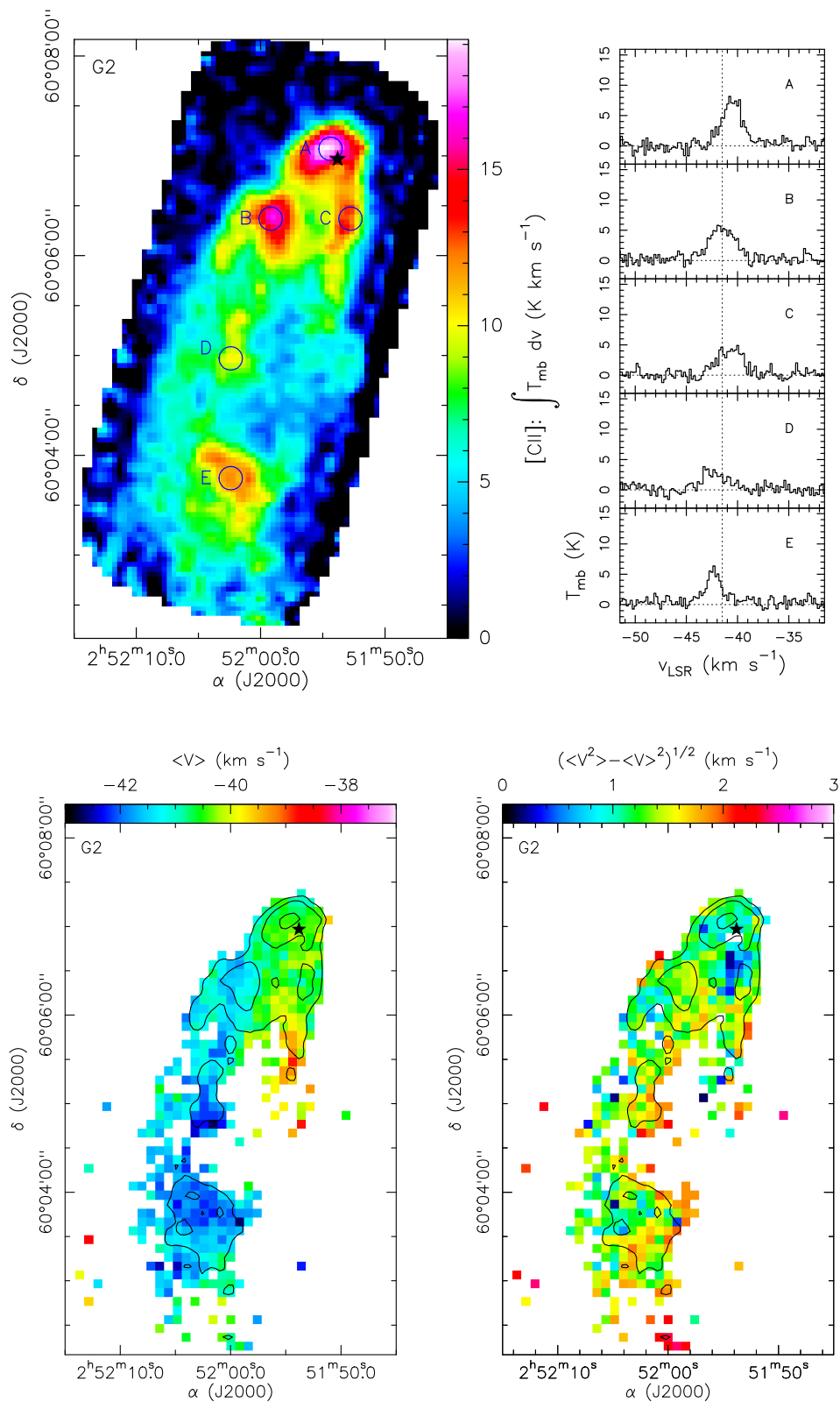


Fig. A.1. (Top) Color image of the [C II] integrated line intensity in the -45 to -37 km s^{-1} velocity range toward the G2 filament. The right panel shows spectra at selected positions labeled A–E in the image. Blue circles correspond to the FWHM SOFIA beam size at the [C II] frequency. (Bottom) Maps of the [C II] line center velocity and velocity dispersion toward the G2 filament (color images, left and right panels, respectively). Only pixels with [C II] intensities above 3.5σ (6.3 K km s^{-1}) are shown. Black contours show the integrated line intensity, with the same contour levels as in Figure 1. Black stars mark the location of the bright IRAC compact source.

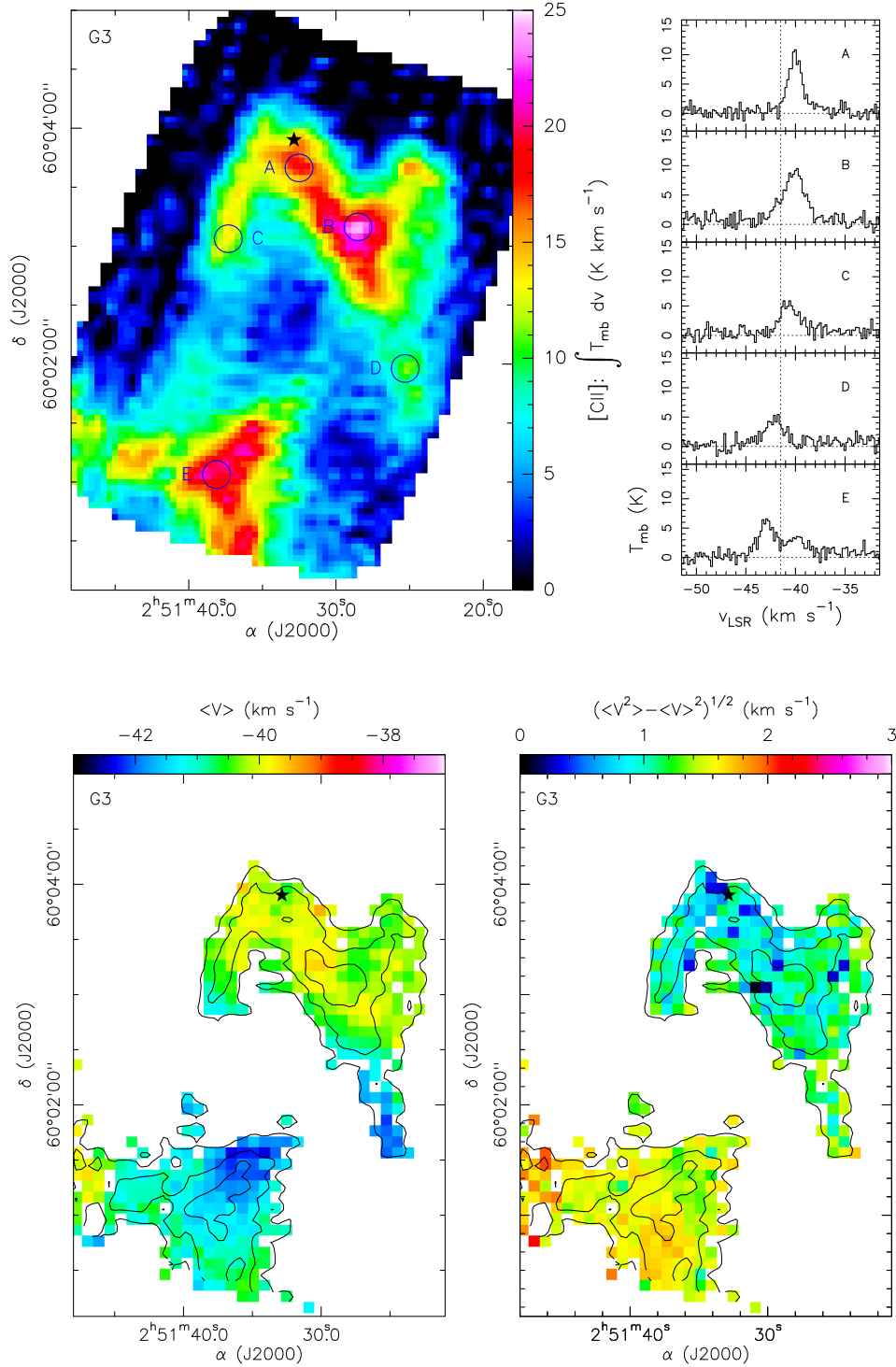


Fig. A.2. (Top) Color image of the [C II] integrated line intensity in the -44 to -38 km s^{-1} velocity range toward the G3 filament. The right panel shows spectra at selected positions labeled A–E in the image. Blue circles correspond to the SOFIA beam at the [C II] frequency. (Bottom) Maps of the [C II] line center velocity and velocity dispersion toward the G2 filament (color images, left and right panels, respectively). Only pixels with [C II] intensities above 3.5σ (8.4 K km s^{-1}) are shown. Black contours show the integrated line intensity, with the same contour levels as in Figure 1. Black stars mark the location of the bright IRAC compact source.

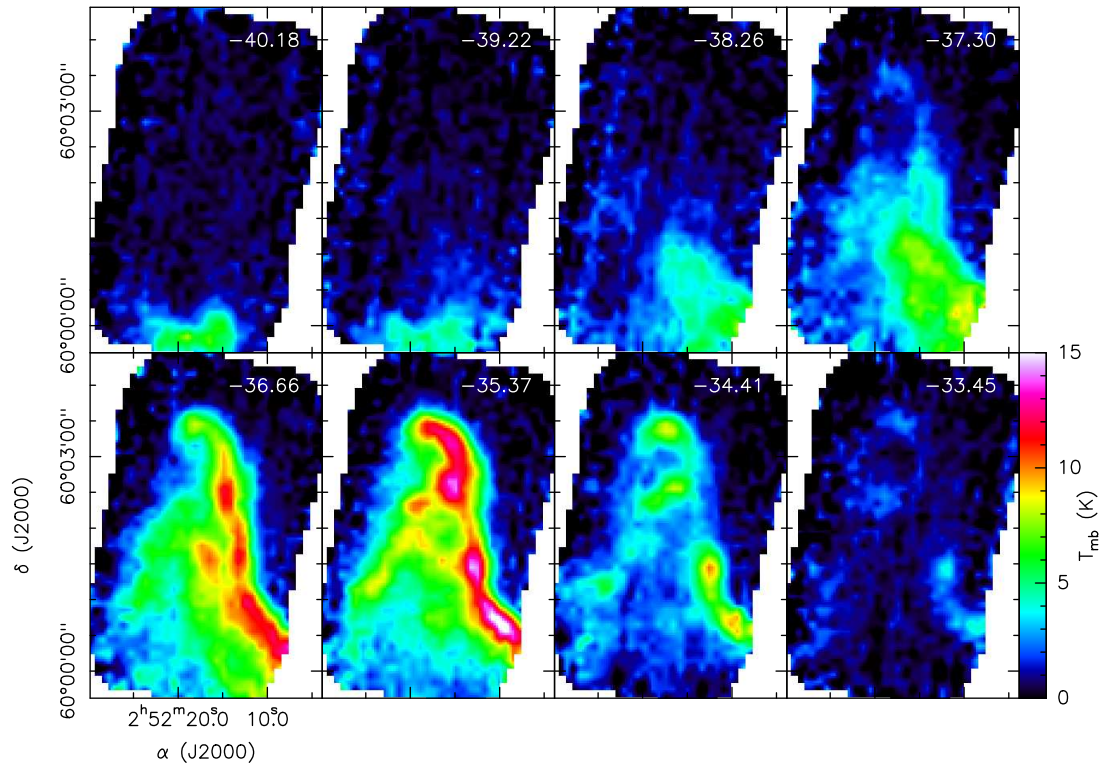


Fig. A.3. Channel maps of the [C II] emission in the G1 filament. Center velocity of each channel is labeled in the upper-right corner.

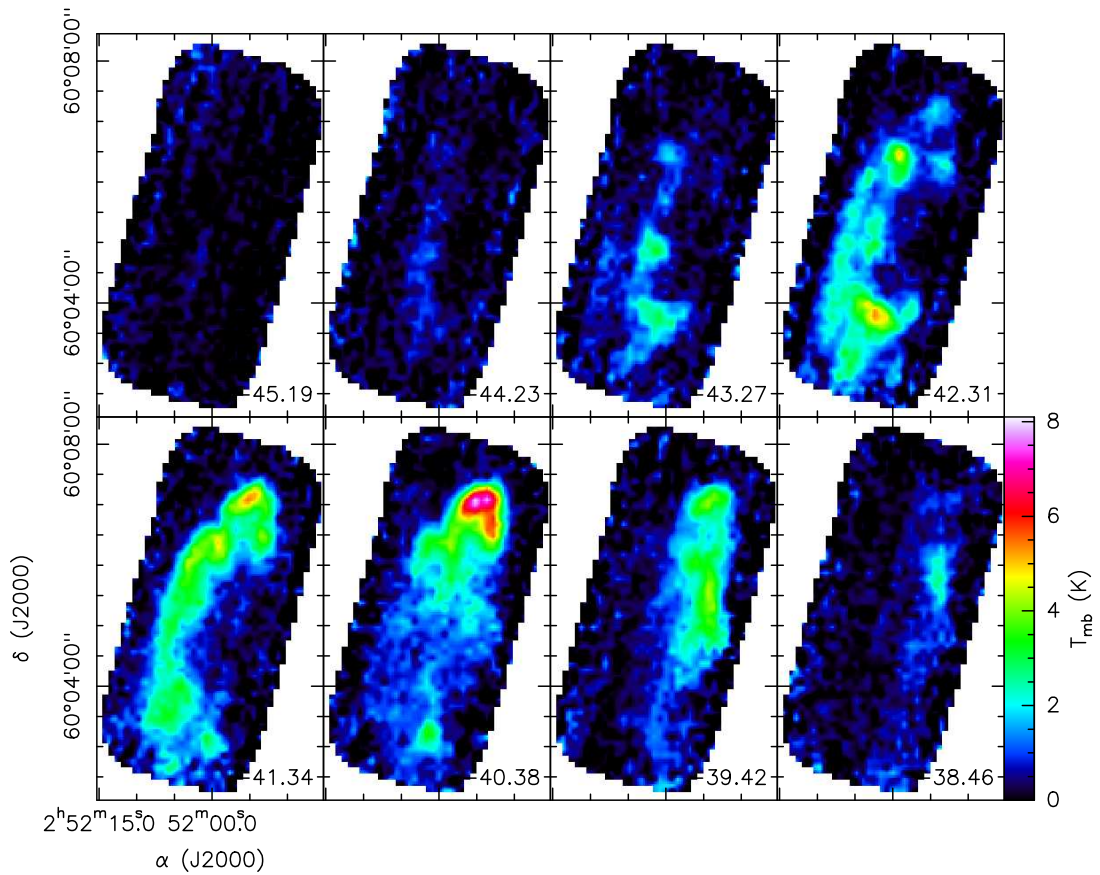


Fig. A.4. Channel maps of the [C II] emission in the G2 filament. Center velocity of each channel is labeled in the lower-right corner.

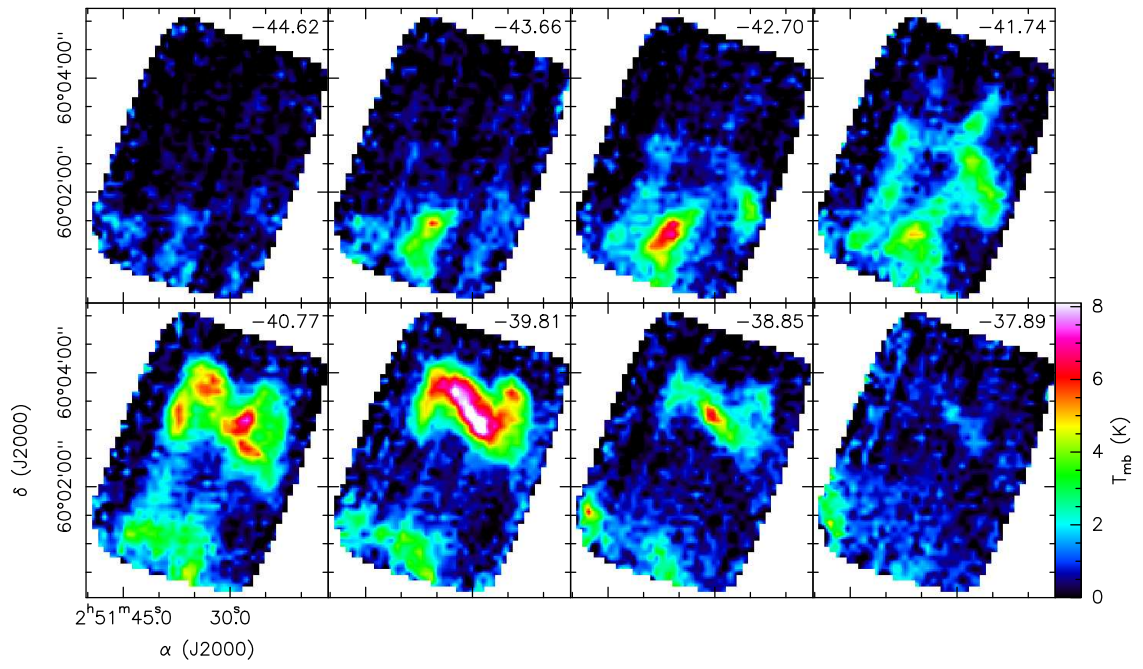


Fig. A.5. Channel maps of the [C II] emission in the G3 filament. Center velocity of each channel is labeled in the upper-right corner.

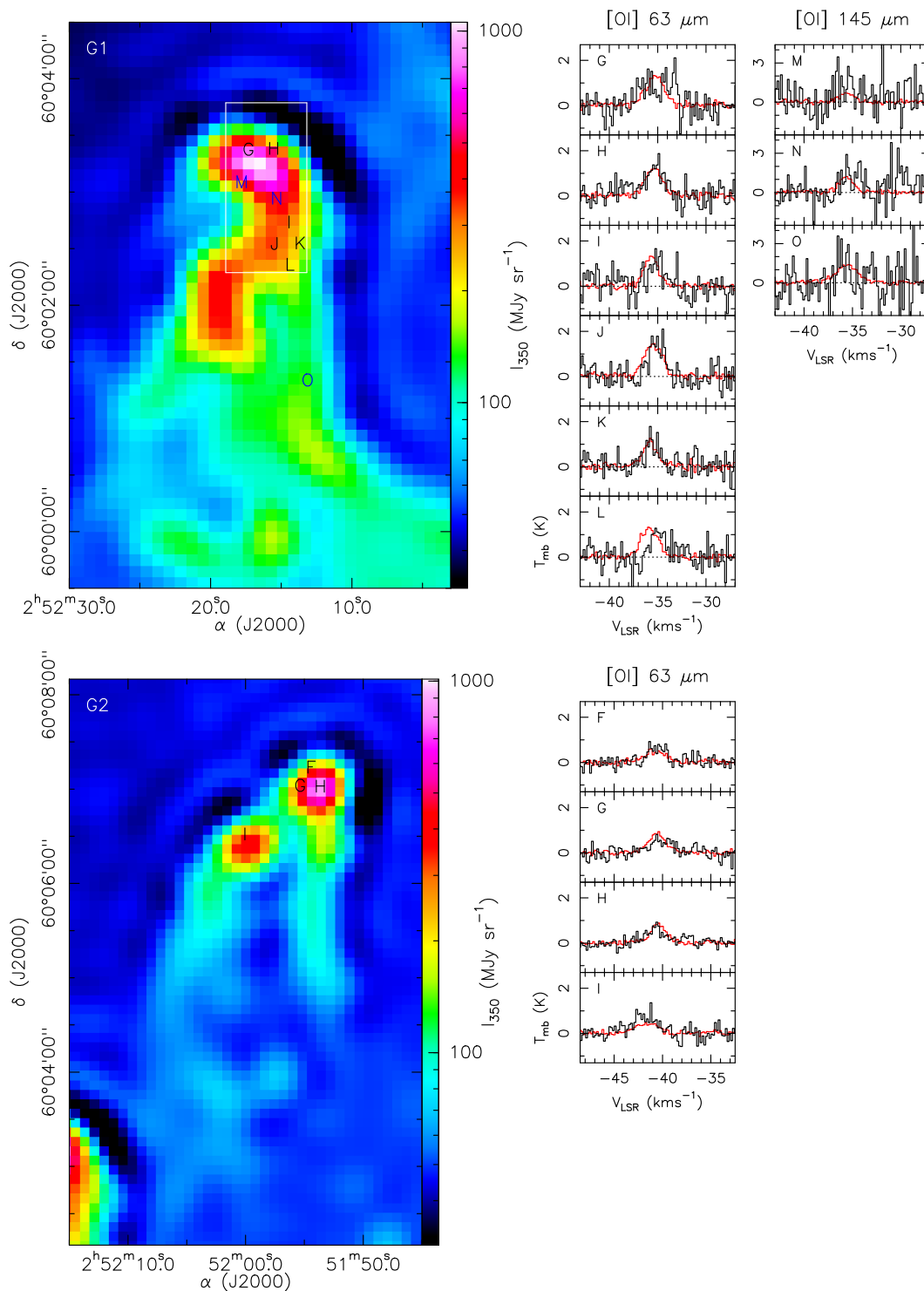


Fig. A.6. [O I] spectra (black histograms) toward positions G–O in the G1 filament (top) and positions F–G in the G2 filament (bottom). Red histograms show the corresponding [C II] spectra divided by 10. Positions at which the spectra are taken are marked on the SPIRE 350 μm images shown in the left panels.

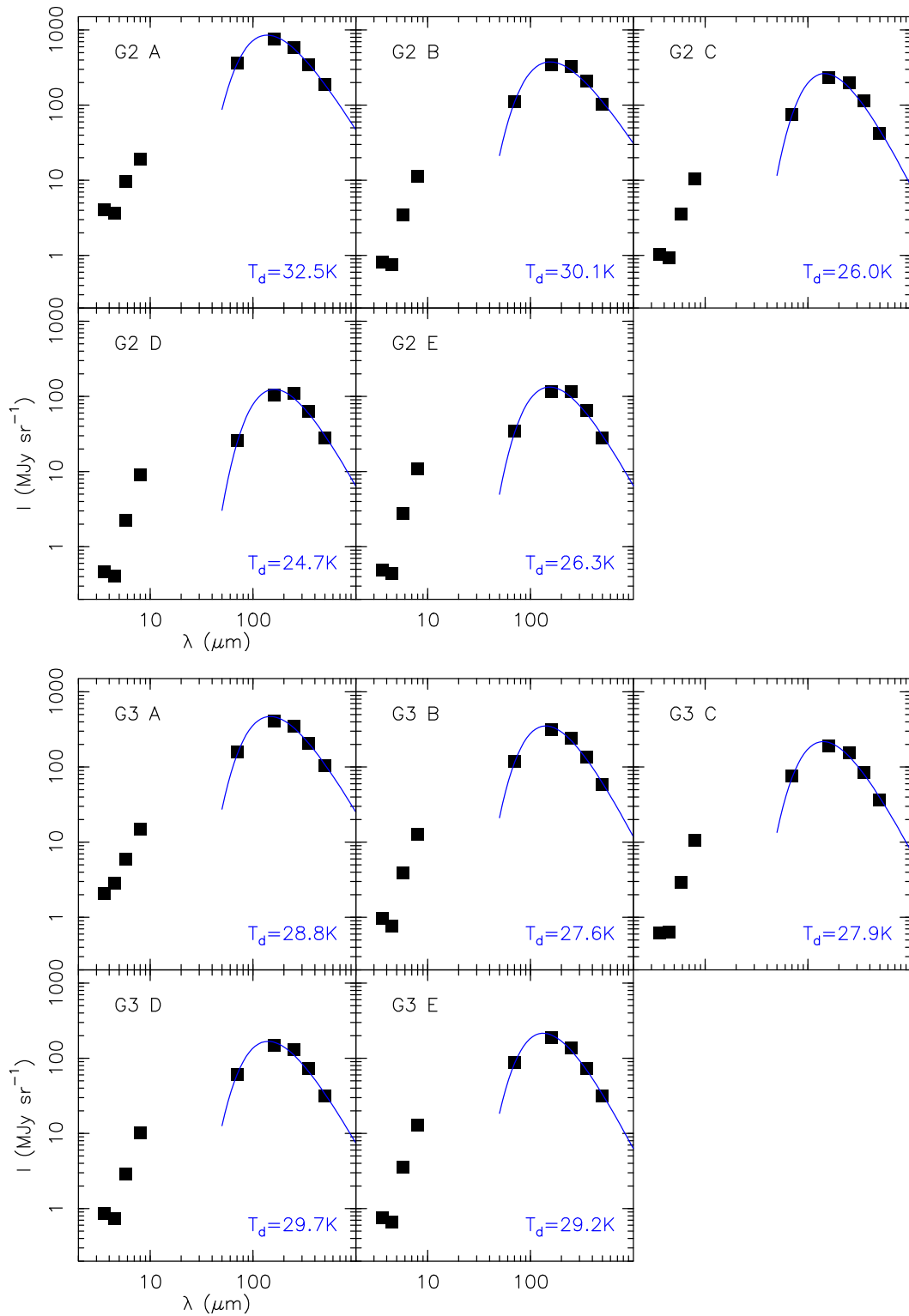


Fig. A.7. Spectral energy distributions toward positions A–E in the G2 and G3 filaments, top and bottom respectively. Blue curves show the modified blackbody fits to the *Herschel* PACS and SPIRE fluxes from which the dust temperatures and 350 μm optical depths used for the column density determination are derived.